Acta Pharmaceutica Sinica B 2026;16(5):3059−3073

Chinese Pharmaceutical Association
Institute of Materia Medica, Chinese Academy of Medical Sciences

Acta Pharmaceutica Sinica B

www.elsevier.com/locate/apsb
www.sciencedirect.com

ORIGINAL ARTICLE

Red blood cell damage defines the etiology of hepatic sinusoidal obstruction syndrome induced by pyrrolizidine alkaloids

Zijing Song[a,†], Yisheng He[b,†], Wei Zhang[c,†], Wei Lian[a], Yueyang Pan[a], Jiang Ma[a], Yuxuan Zhao[b], Tianyang Huang[b], Yuzheng Zhuge[c,*], Ge Lin[a,*]

[a]*School of Biomedical Sciences, Faculty of Medicine, The Chinese University of Hong Kong, Hong Kong, China*
[b]*School of Medicine, The Chinese University of Hong Kong, Shenzhen 518172, China*
[c]*Department of Gastroenterology, Nanjing Drum Tower Hospital, The Affiliated Hospital of Nanjing University School of Medicine, Nanjing 210008, China*

Received 10 May 2025; received in revised form 1 August 2025; accepted 13 November 2025

KEY WORDS

Liver sinusoidal endothelial cells;
Red blood cells;
Hemolysis;
Hemoglobin;
Pyrrole−haptoglobin adducts;
Blood−liver axis;
Hepatic sinusoidal obstruction syndrome;
Etiological therapy

Abstract Hepatic sinusoidal obstruction syndrome (HSOS), a life-threatening liver disease characterized by sinusoidal endothelial cell (LSEC) damage, is frequently caused by pyrrolizidine alkaloid (PA) exposure present in numerous herb or food products. Unlike other hepatotoxins, the precise mechanism by which PAs selectively target LSECs remains poorly understood, posing significant challenges to the development of effective treatments. This study identified hemolysis as the initiating event in PA-HSOS pathogenesis through clinical and animal model analyses. PA exposure induced red blood cell (RBC) rupture, releasing free hemoglobin (Hb) that directly damaged LSECs. Mechanistic investigations revealed that PA-formed protein adducts with haptoglobin (Hp), impairing its protective effect against toxic Hb and triggering a cascade of LSEC activation, ferroptosis, and hemorrhagic liver necrosis. Rescue study revealed that Hp supplementation effectively mitigated PA-induced liver injury by scavenging free Hb. Clinical validation demonstrated elevated Hb−Hp adducts and cell-free Hb in PA-HSOS patients, confirming concordant intoxication mechanisms across species. The findings redefine PA-HSOS as a hematogenous liver disorder originating from RBC destabilization, rather than direct hepatocyte toxicity. This hematopathological perspective reveals Hp replacement therapy as a promising etiological treatment strategy, addressing the root cause rather than secondary liver damage.

*Corresponding authors.
E-mail addresses: yuzheng9111963@aliyun.com (Yuzheng Zhuge), linge@cuhk.edu.hk (Ge Lin).
†These authors made equal contributions to this work.

Peer review under the responsibility of Chinese Pharmaceutical Association and Institute of Materia Medica, Chinese Academy of Medical Sciences.

https://doi.org/10.1016/j.apsb.2026.03.023

1. Introduction

Hepatic sinusoidal obstruction syndrome (HSOS) is a fatal vascular liver disease initiated by injury of liver sinusoidal endothelial cells (LSECs), followed by sinusoid congestion and hemorrhagic hepatocyte necrosis, eventually leading to liver failure[1,2]. In particular, most HSOS cases represent the distinct manifestation of drug-induced liver injury (DILI), because the common causes of HSOS include chemotherapy used in bone marrow transplantation and pyrrolizidine alkaloids (PAs) contained in various herbal remedies[3-6]. Of note, due to the ubiquitous distribution of PA-producing plants[7], people more often and unavoidably exposed to PAs. For instance, PAs have been detected in 94% of retail honey samples in European markets according to a large-scale survey[8]. Outbreaks of PA poisoning cases, with thousands of reported deaths, have been documented in many countries, such as Afghanistan[9], Ethiopia[10], Tajikistan[11], and India[12], most of which were caused by the intake of grains contaminated by PA-producing plants. While in China with prevalent self-medication, PA-induced HSOS (PA-HSOS) due to the misuse of PA-containing herbal medicine *Gynura Japonica* represents the characterized herb-induced liver injury (HILI)[6,13].

The biochemical basis of PA intoxication is similar to many other hepatotoxic reagents such as acetaminophen: the hepatic metabolic activation and protein adduction. Upon exposure, PAs are metabolically activated by hepatic cytochrome P450 enzymes (CYPs) to produce dehydro-pyrrolizidine alkaloids (DHPA) (Supporting Information Fig. S1)[14]. The reactive DHPAs then covalently bind to biological proteins and form pyrrole−protein adducts (PPAs), thereby causing protein defunction and cytotoxicity. Our group has developed PPAs as mechanism-based biomarkers of PA intoxication, together with clinically actionable blood testing approaches, our method enables a definitive diagnosis of human PA-HSOS[15-17]. However, current HSOS therapies are limited to anticoagulation treatments that address symptoms with unsatisfactory outcomes[18]. Therefore, based on the common biochemical protein adduction mechanism, identifying the unique protein targets that are responsible for PAs' characteristic toxic effect on LSECs is the key to develop etiological therapy for effective treatment PA-HSOS.

Of note, when applying PPA detection for PA-HSOS diagnosis, we repeatedly found that PA exposure preferentially produces PPA in red blood cells (RBCs), with the level significantly higher than that in plasma and even liver where PAs are metabolically activated[19,20]. This unique capability to form RBCs protein adducts is rarely observed with other hepatotoxic reagents such as acetaminophen, leading us to hypothesize that RBC PPAs and resultant RBC damage might be crucial mediating PA-induced LSEC damage. It is noteworthy that rupture of RBCs, *i.e*., hemolysis, has been extensively reported as a common cause of vascular endothelial damage[21,22]. Considering that LSEC damage is the initiating event of HSOS, we thus hypothesized that PPAs formation in RBCs leads to intrahepatic RBC rupture. Subsequently, the accumulation of toxic hemolytic products damages LSECs, initiating the pathogenesis of HSOS.

In this study, we first investigated the hemolytic event in PA-HSOS patients, who mainly underwent tests related to hepatic functions. We then examined PA-induced RBC rupture in experimental PA-HSOS models. Further, we identified that haptoglobin (Hp), the plasma scavenger for hemoglobin (Hb, the main hemolytic product), was another protein target of DHPA adduction. Loss-of-function test was performed to confirm that defunctioning Hp caused the accumulation of Hb and hemolytic iron overload, directly damaging LSECs and subsequently hepatocytes. Furthermore, blood samples from PA-HSOS patients were analyzed to verify the identified blood protein adducts and the clinical relevance. Finally, by supplementing exogenous Hp, we aimed to support our hypothesis that hemolysis is the initiating event of PA-induced LSEC damage and HSOS, proposing that hemolytic product clearance could serve as the etiological therapy to effectively treat PA-HSOS.

2. Materials and methods

2.1. Human samples and patient cohorts

This study recruited thirty PA-HSOS patients admitted between April 2019 to July 2020 at Nanjing Drum Tower Hospital, Nanjing, China. Written informed consent was obtained from all participants, adhering to the ethical principles outlined in the Declaration of Helsinki and Good Clinical Practice guidelines. This study was approved by the ethics committee of Nanjing Drum Tower Hospital (Approval No. 2018-272). A summary of the clinical characteristics of the enrolled patients is provided in Table 1. Human plasma samples for biochemical examinations were derived from all 30 PA-HSOS patients. Plasma hemoglobin (Hb), ferritin, transferrin receptor (TFR), and pyrrole−haptoglobin (Hp) adducts were analyzed.

2.2. Animal experiments

2.2.1. Animal ethical guidelines

Male Sprague−Dawley (SD) rats (6−8 weeks) and male C57BL/6 (C57) mice (6−8 weeks) supplied by the Laboratory Animal Services Centre at The Chinese University of Hong Kong (CUHK) were housed in the animal holding room with a 12-h dark/light cycle, 18−25 °C, and 55 ± 5% humidity-controlled environment. All animals were cared for in compliance with the regulations of the Laboratory Animal Service Center, CUHK. Both housing conditions and experimental procedures were reviewed and approved by the Animal Experimental Ethics Committee (AEEC. No. 19/064/GRF and 20/030/GRF) at CUHK, in accordance with the regulations of the Hong Kong SAR government.

2.2.2. Rat model

Whole blood samples were collected from normal SD rats and 200 μL whole blood samples were incubated with 0.4 μL MCT, RTS, and DHM, respectively to make the final concentration at 117.55 μmol/L. Additionally, 0.4 μL DMSO was incubated with 200 μL whole blood as parallel control. MCT, RTS, and DHM were dissolved in DMSO at 58.78 mmol/L. The RBCs and plasma

Table 1 Information of 30 PA-HSOS patients due to PA-exposure.

Patient ID	Sex	Age	Herb ingested	Intake dose/period	Jaundice/ascites/hepatomegaly
001	M	67	Liquor	<2 months	Y/Y/N
002	F	65	Tea	3 months	Y/Y/Y
003	M	63	Powder	4 months	Y/Y/Y
004	M	72	Powder	300 capsules/2 months	Y/Y/N
005	M	69	Powder	1−2 g/day, 3 months	N/Y/N
006	F	77	Unknown	Unknown	N/Y/Y
007	M	69	Tea	7 days	Y/Y/N
008	F	52	Tea	1 year	N/Y/N
009	M	47	Tea	<1 month	Y/Y/N
010	M	69	Tea	1.5 month	Y/Y/N
011	M	55	Tea	50 days	N/Y/Y
012	M	74	Tea	3 days	N/Y/Y
013	M	63	Liquor	1 month	N/Y/N
014	M	50	Tea	Half months	N/Y/Y
015	M	71	Unknown	Unknown	N/Y/Y
016	M	65	Liquor	<1 month	N/Y/N
017	M	53	Liquor	20 days	N/Y/N
018	F	69	Decoction	4 times	Y/Y/Y
019	F	55	Tea	50 days	N/Y/N
020	M	51	Tea	1 month	N/Y/Y
021	M	58	Tea	3−4 g/day, 1 month	N/Y/N
022	M	66	Tea	Known	Y/Y/Y
023	M	68	Tea	2 months	N/Y/Y
024	F	70	Tea	1 month	Y/Y/Y
025	M	71	Tea	Half years	Y/Y/N
026	F	63	Liquor	1.5 kg	N/Y/Y
027	M	63	Tea	4 days	Y/Y/N
028	M	62	Decoction	1 week/year, 10 years	Y/Y/N
029	M	21	Tea	3 months	Y/Y/N
030	F	63	Decoction	3 times	Y/Y/N

were separated by centrifugation at 3000 rpm for 10 min. Plasma Hb level, plasma and RBC PPA levels were determined respectively.

SD rats were randomly divided into two groups (n = 3/group) for monocrotaline (MCT) or retrorsine (RTS) treated groups. Rats in two groups were administered intravenously with a single dose (0.2 mmol/kg) of MCT or RTS. MCT and RTS were dissolved in distilled water acidified by 1.0 mol/L hydrochloric acid, and then adjusted pH to 7.0 with 1.0 mol/L sodium hydroxide. Blood samples were collected from the left ventricle of individual rats at 3 min, 1, 4, and 12 h after PA administration, respectively, for morphological analysis using a scanning electron microscope (SEM). Blood samples collected from rats without PA treatment were used as control RBCs.

2.2.3. Mouse model

In order to determine the dosages of RTS treatment, mice were administered a single dose of RTS at 40, 50, 60, and 70 mg/kg per oral. Blood samples were collected at 48 h post dose. Plasma ALT activity was determined as an indicator of liver damage. As results shown (Supporting Information Fig. S2), at a dose of 40 mg/kg, RTS did not cause obvious liver damage, while at 70 mg/kg, RTS induced excessively severe liver damage (one mouse died before the endpoint). Doses of 50 and 60 mg/kg of RTS resulted in mild and relatively severe HSOS, respectively. Therefore, in subsequent experiments, mice treated with 50 and 60 mg/kg of RTS were used as models for mild and severe PA-HSOS, respectively.

To study RTS-induced hematopathy, C57 mice were randomly divided into control and the RTS-treated groups. Mice were orally administered a single dose of RTS (60 mg/kg). Blood samples were collected from tail vein at 3, 6, 9, 24 and 48 h after RTS administration for blood smear preparation, while blood samples collected before RTS administration were used as control blood smear.

To study glucose-6-phosphate dehydrogenase (G6PD) function, C57 mice were randomly divided into control and the RTS-treated groups. Mice in different groups were orally administered a single dose of RTS (60 mg/kg) or vehicle, respectively. At 3, 12, 24, and 48 h after RTS administration, three mice from individual RTS-treated group were sacrificed respectively. Blood samples were collected and tested for G6PD activity immediately.

For pyrrole−protein adducts identification, C57 mice were randomly divided into control and RTS-treated groups (n = 3/group). Mice in different groups were orally administered a single dose of RTS (60 mg/kg) or vehicle, respectively. Mice were sacrificed at 3 h after RTS administration. Liver samples were collected for the analysis.

For pathogenesis study, C57 mice were randomly divided into control, RTS-50 and RTS-60 groups (n = 3/group). Mice in different groups were orally administered a single dose of RTS at 50 or 60 mg/kg or vehicle, respectively. At 3, 12, 24, and 48 h after RTS administration, mice from RTS-50 and RTS-60 groups were sacrificed, respectively. Blood and liver samples were collected for histological and biochemical examinations.

To investigate RTS-induced ferroptosis. Mice were divided into RTS and RTS + Lip-1 groups (n = 5/group). Mice were orally administered a single dose of RTS (50 mg/kg). Four doses of liproxstatin-1 (Lip-1) (at 3, 9, 27, and 33 h after RTS treatment)

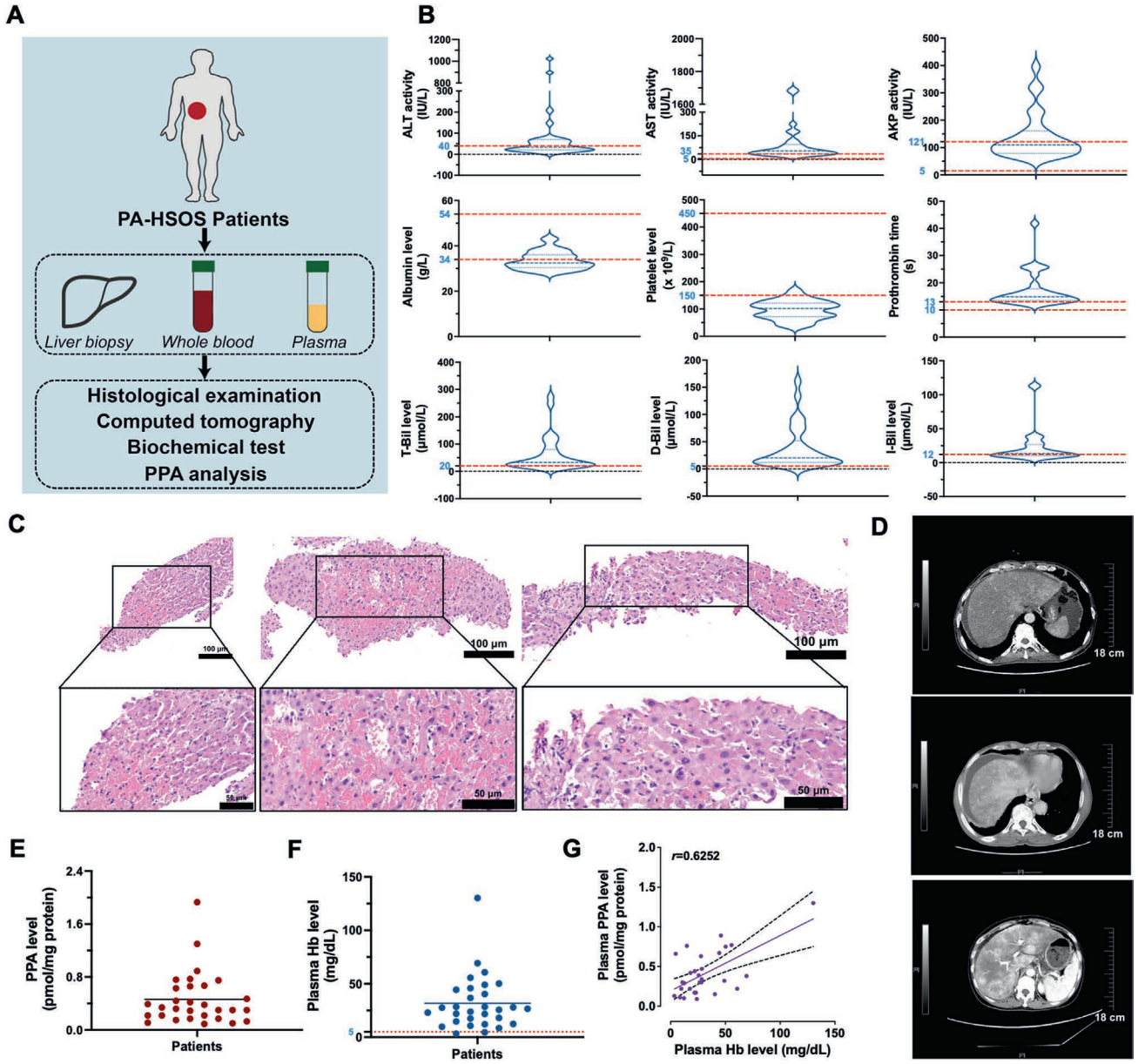

Figure 1 Hematopathy in PA-induced HSOS patients. (A) Schematic process of experimental design. (B) Violin plots of physiological indices. The boxplots showing median, and 1st and 3rd quartiles of the predictor variables are overlayed on the violin plots. (C) Representative H&E staining and (D) representative CT images of liver. (E) Plasma pyrrole−protein adduct level. (F) Plasma Hb level. (G) Results of correlation analysis (n = 29 patients) (Simple logistic regression and Pearson correlation analysis). Data are expressed in scatter dot plots of individual data points with mean indicated in blue line (n = 30 patients). Normal ranges/limits are indicated by red dashed lines. Bars represent 100 μm (C) and 18 cm (D).

were given intraperitoneally to the mice at 100 mg/kg/dose. Mice were sacrificed at 48 h after RTS treatment. Blood and liver samples were collected for biochemical and histological examinations.

For the therapeutic study with Hp supplements, mice were divided into five groups: control, RTS-50, RTS-50+Hp, RTS-60, and RTS-60+Hp groups (n = 5/group). Mice were orally administered with a single dose of RTS at 50 or 60 mg/kg or vehicle. Two (3 and 9 h after RTS treatment) or four doses (3, 9, 27, and 33 h after RTS treatment) of Hp (200 μg/mouse/dose) were given intraperitoneally to mice in RTS-50+Hp and RTS-60+Hp group, respectively. At 48 h after RTS treatment, mice were sacrificed respectively. Blood, liver, and spleen samples were collected for histological and biochemical examinations.

2.3. *In vitro experiments*

2.3.1. *Incubation of DHM with Hp*

To obtain Hp−pyrrole adducts, 50 μL Hp solution (1.5 mg/mL) was incubated with 5 μL DHM (19 mg/mL) or DMSO for 5 min at 37 °C, respectively. Then, 50 μL Hb solution (3 mg/mL) was added and incubated for 1 h at 37 °C. The obtained solutions were used for Hp lose-of-function study.

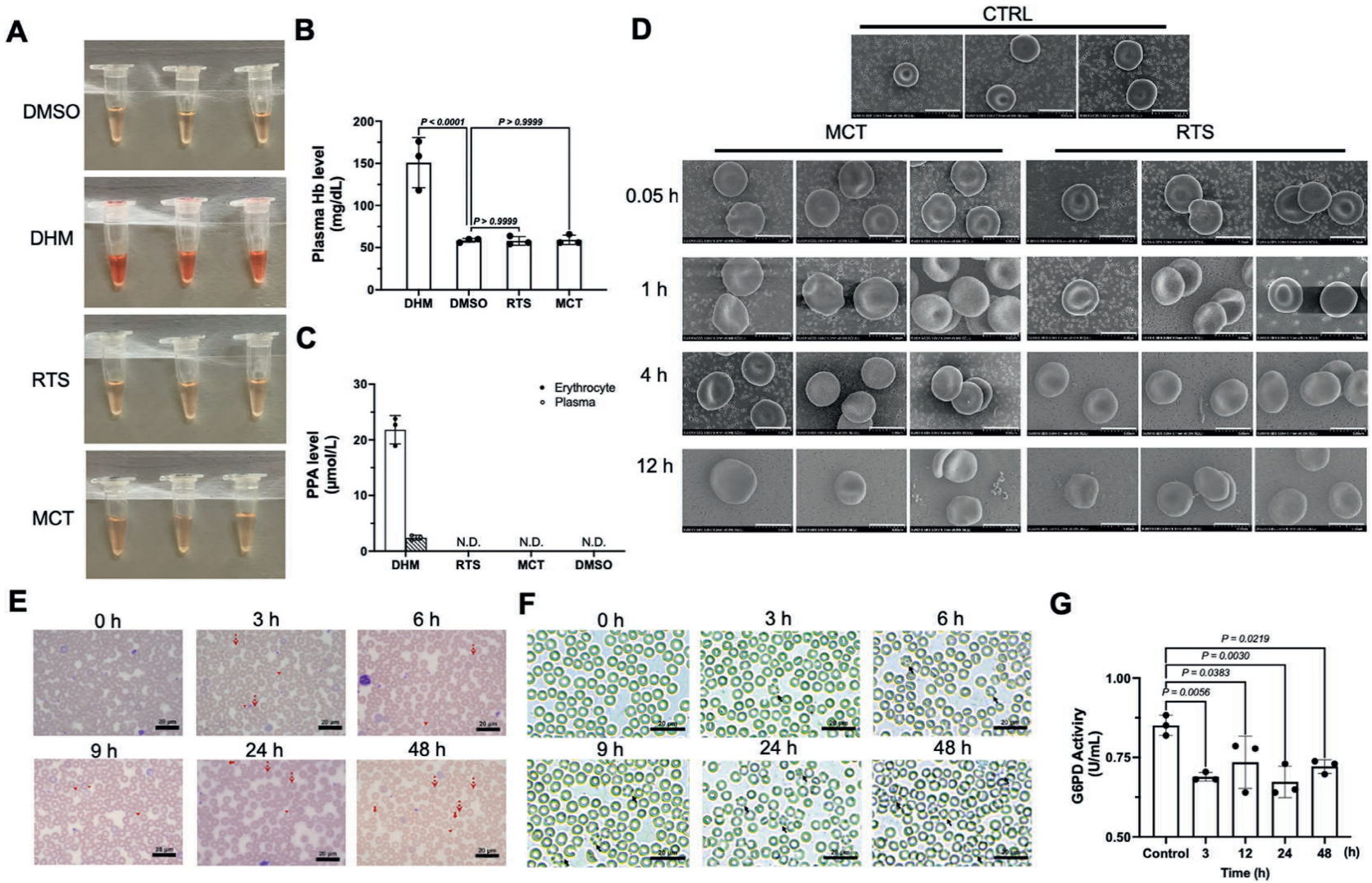

Figure 2 PA-induced hematopathy in experimental animals. (A) Separated plasma samples of whole blood exposed to DMSO, DHM, MCT or RTS (117.55 μmol/L). (B) Plasma Hb level after exposure to DMSO, DHM, MCT or RTS (117.55 μmol/L). (C) Pyrrole−protein adduct level of plasma and RBCs after exposure to DHM (117.55 μmol/L). (D) Morphology of rat RBCs following MCT or RTS exposure. (E) Wright−Giemsa staining of mouse blood smear following RTS exposure: "blister" and "bite" cells (⬇), microcytic cells (▲), spherocytes (↑). (F) Heinz body staining of mouse blood smear following RTS exposure: Heinz body (⬇). (G) RBC G6PD activity in mice following RTS exposure (n = 3/group) (One-way ANOVA analysis). Data are expressed as mean ± SD. Bars represent 5 μm (D) and 20 μm (E, F).

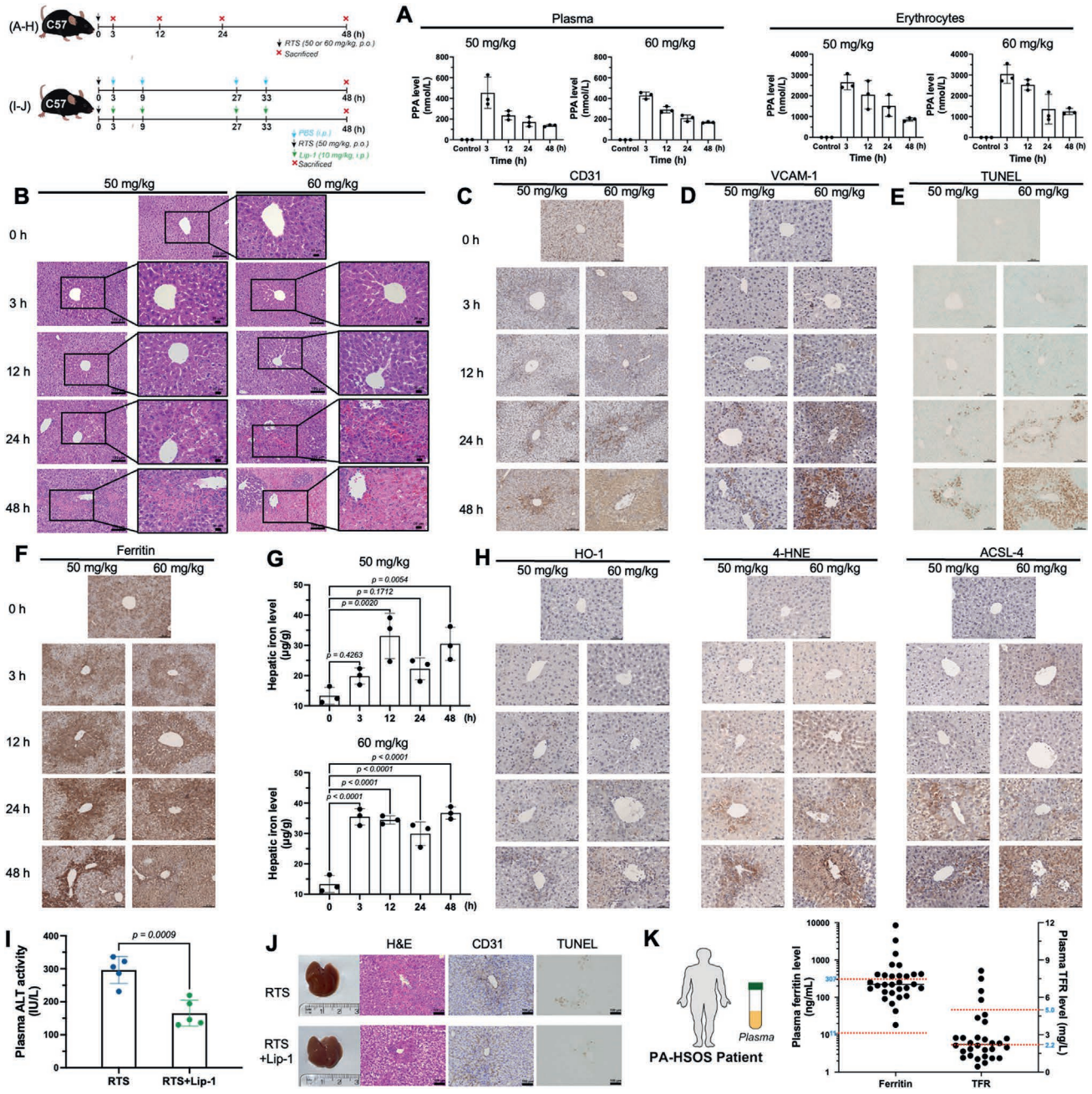

Figure 3 Progression of HSOS initiated by PA-induced hemolysis in mice and iron overload in PA-HSOS patients. (A) Levels of PPA (n = 3/group). Representative images of H&E staining (B), IHC staining of CD31 (C) and VCAM-1 (D), TUNEL (E), IHC staining of ferritin (F) in liver. (G) Hepatic non-protein-bound iron levels (n = 3/group) (One-way ANOVA analysis). (H) Representative images of IHC staining of HO-1, 4-HNE and ACSL-4 in liver. (I) Plasma ALT activity (n = 5/group) (Student's t-test). (J) Representative images of H&E staining, IHC staining of CD31 and TUNEL. (K) Plasma ferritin and transferrin receptor levels (n = 30 patients). Normal ranges/limits are indicated by red dashed lines. Data are expressed as mean ± SD. Bars represent 20 or 100 μm (B), 100 μm (C, E, F, J), and 50 μm (D, H).

2.3.2. Cell culture and treatment

Human hepatic sinusoidal endothelial cells (HSECs) were obtained from ScienCell Research Laboratories (CA, USA). HSECs were cultured in an endothelial cell medium supplemented with 5% FBS and 1% endothelial cell growth supplement according to the manufacturer's protocol. To investigate toxicity of cell-free Hb, HSECs were seeded in a 96-well plate and cultured with 1 mg/mL Hb in a Hb/H_2O_2 system (20 mU/mL GOx and 4 mg/mL glucose)[23] for 3, 9, and 12 h, respectively. To investigate protective effect of Hp against toxicity of cell-free Hb, HSECs were seeded in 96-well plates and cultured with 1 mg/mL Hb in a Hb/H_2O_2 system with or without 1 mg/mL Hp for 24 h. Vehicle control was conducted in parallel. Cell viability of HSECs was measured using cell counting kit-8 (MedChemExpress, Cat. #HY-K0301) following the manufacturer's instruction.

The human hepatic cell line HepaRG was obtained from Bioperdic International (Rennes, France). HepaRG cells were cultured in a HepaRG growth medium consisting of basal

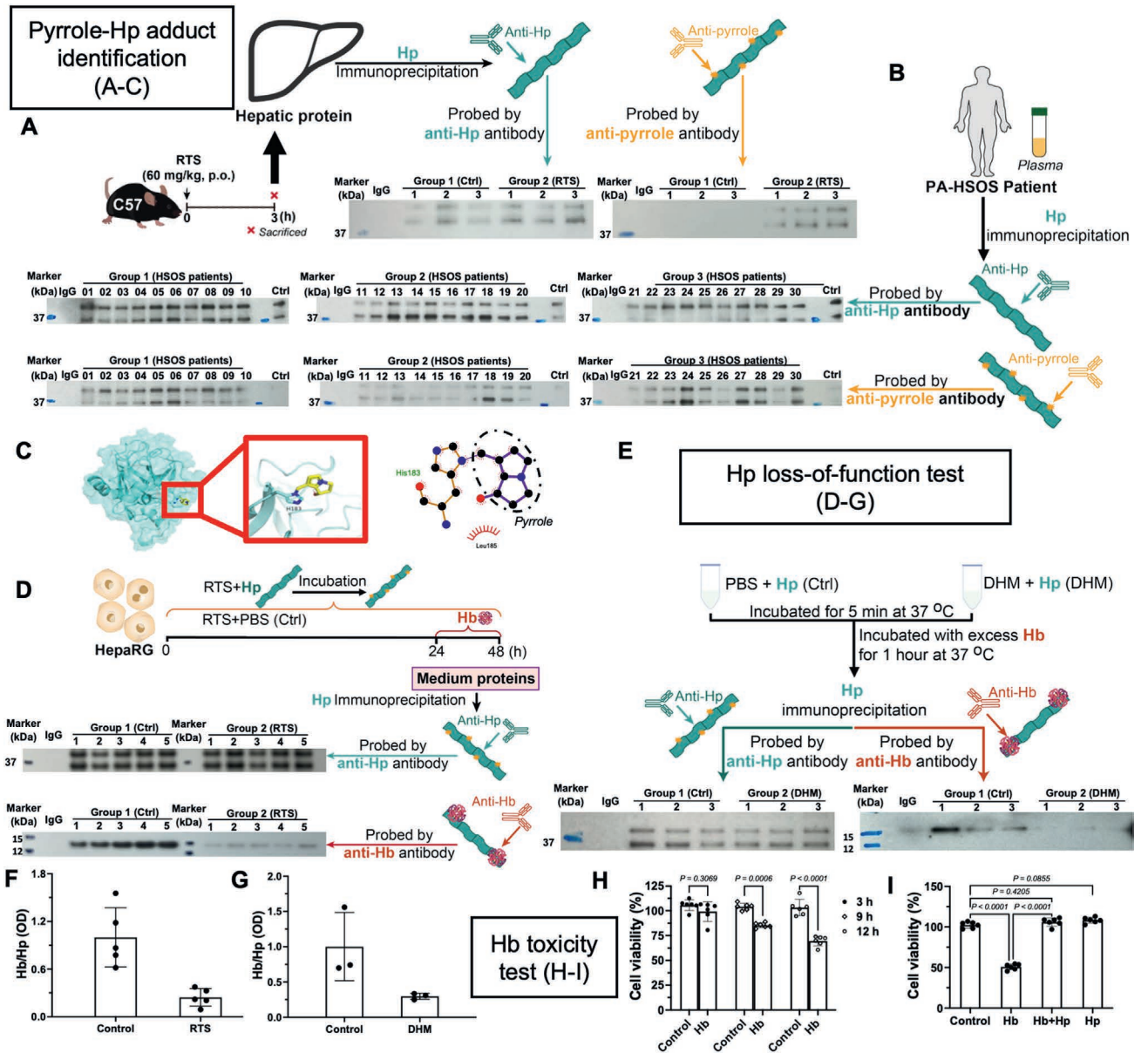

Figure 4 PA-induced pyrrole−haptoglobin adduct formation and resulting compromised hemoglobin clearance. (A) Hepatic expression of pyrrole−Hp adducts at 3 h after RTS exposure to mice. (B) Plasma expression of pyrrole−Hp adducts in PA-HSOS patients. (C) Covalent docking of pyrrole interaction with Hp. (D) Altered Hb−Hp complex formation and OD ratio of Hb to Hp (F) after RTS exposure to HepaRG cells ($n = 3$) (Student's *t*-test). (E) Altered Hb−Hp complex formation and OD ratio of Hb to Hp (G) after Hp exposed to DHM ($n = 3$) (Student's *t*-test.) (H) Cell-free Hb-induced (1 mg/mL) toxicity to human LSECs after incubation for 3, 9, or 12 h ($n = 6$/group) (Student's *t*-test). (I) Hp (1 mg/mL) reduced Hb-induced (1 mg/mL) toxicity to human LSECs after incubation for 24 h ($n = 6$/group) (One-way ANOVA analysis). Data are expressed as mean ± SD.

Williams' E medium supplemented with 10% fetal bovine serum (FBS), 50 units/mL penicillin, 50 μg/mL streptomycin (Thermo Fisher Scientific), 5 μg/mL insulin (Sigma−Aldrich), 2 mmol/L glutaMAX (Thermo Fisher Scientific), and 50 μmol/L hydrocortisone hemisuccinate (Sigma−Aldrich) using Biopredic's protocol[24]. Briefly, the cells were cultivated in HepaRG growth medium in a T75 flask for 2 weeks. Then, cells were harvested and seeded onto 6-well plates at a density of 2.5×10^5 cells/well. After 2 weeks, the cells were incubated with a differentiation medium containing 1.5% (*v*/*v*) dimethyl sulfoxide for additional 2 weeks. Hp (0.12 mg/mL) was incubated with differentiated HepaRG cells, with or without RTS (240 μmol/L), in an FBS-free differentiation medium for 24 h. Then, Hb was added into the medium at a final concentration of 0.36 mg/mL and cultured for 1 h at 37 °C. The medium samples were collected for pyrrole−protein adduct (PPA) measurement and co-immunoprecipitation (Co-IP).

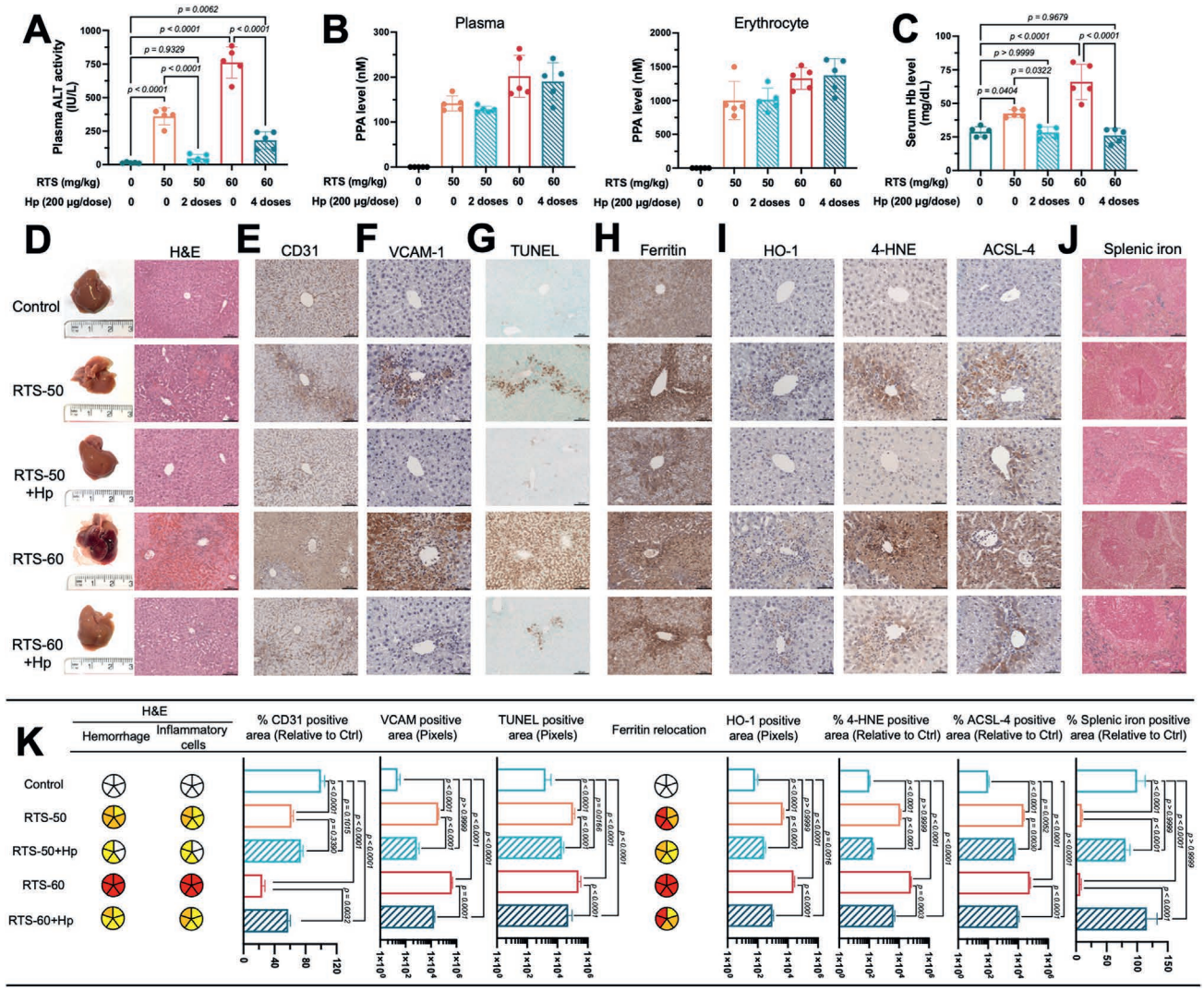

Figure 5 Haptoglobin supplement is an etiological therapy effectively against PA-induced HSOS in mice. (A) ALT activity. (B) PPA levels in plasma and RBCs. (C) Plasma Hb level. Data are expressed as mean ± SD (n = 5/group) (One-way ANOVA analysis). Representative images of H&E staining (D) and IHC staining of CD31 (E) and VCAM-1 (F); TUNEL (G); IHC staining of ferritin (H) and HO-1, 4-HNE, and ACSL-4 (I) in liver. (J) Perls' Prussian blue staining of splenic iron. (K) Semi-quantification of histological results. Data are presented as mean ± SEM (n = 5/group) or histology pies. Each pie is divided into slices equal to the number of rats comprising the group. Slices are colored according to histology score; each parameter is graded on the four-point system: 0−absent (white), 1−mild (yellow), 2−moderate (orange), and 3−severe (red). Bars represent 100 μm (D, E, G, H, J) and 50 μm (F, I).

2.3.3. *Biochemical assays*

For mouse samples, plasma ALT activity was determined by EnzyChrom™ alanine transaminase assay kit (BioAssay System, Cat. #EALT-100). Mouse serum Hb levels were determined by QuantiChrom™ hemoglobin assay kit (BioAssay System, Cat. #DIHB-250). For mouse hepatic non-protein iron level measurement, liver homogenates were prepared from RTS-exposed and control mice. The supernatant was collected after centrifugation at 10,000 rpm for 10 min at 4 °C. To precipitate proteins, 150 μL of methanol were mixed with 50 μL of the supernatant. The mixture was centrifuged at 10,000 rpm for 10 min at 4 °C, and 50 μL of the supernatant were taken for measurement of the hepatic non-protein iron level using QuantiChrom™ iron assay kit (BioAssay System, Cat. #DIFE-250).

For PA-HSOS patient samples, patient plasma Hb levels were measured by QuantiChromTM hemoglobin assay kit (BioAssay System, Cat. #DIHB-250). Plasma ferritin levels were determined by Human ferritin ELISA kit (Thermo Fisher, Cat. #EHFTL). Plasma transferrin receptor levels were determined by human transferrin receptor ELISA kit (Solarbio, Cat. #SEKH-0330).

2.3.4. *Pyrrole−protein adduct measurement*

Pyrrole−protein adduct levels in patient plasma, mouse plasma and RBC, and HepaRG cell medium were measured according to our previously reported method using ultra-high performance liquid chromatography-mass spectrometry (UHPLC−MS)[15].

2.4. Histological examinations

2.4.1. SEM analysis

Rat blood samples (about 10 μL) collected at the designed time points were immediately transferred to 2.0 mL of fixative buffer [70 mmol/L $(CH_3)_2AsO_2Na$, 3 mmol/L $MgCl_2$, pH 7.2, 290 mOsm/L] containing 1.6% glutaraldehyde. After fixing RBCs at 4 °C for 2 h, the specimens were dropped on the membrane with 2.5 μL per site. The membrane was air-dried overnight for adhesion of RBCs, followed by gently washing with distilled water 3 times. Subsequently, the specimens were dehydrated sequentially in 75%, 85%, 95%, and 100% ethanol solutions. The samples were mounted on the surface of the copper stub and sputter-coated with gold. The morphology of RBCs was examined and photographed using Hitachi SU8010 scanning electron microscope with an iXRF EDS system.

2.4.2. Wright-Giemsa staining of blood smear

Following the manufacturer's instruction, blood smears were stained with a Wright-Giemsa staining kit (BASO Diagnostics, Cat. #BA4017). The smears were examined with Nikon Ni-U Eclipse upright microscope imaging system using a color camera and manual stitching function.

2.4.3. Heinz body staining of blood smear

Dropping methylene blue stain onto a glass slide and allowing it to dry. Fresh blood is then smeared across the slide, after which it is stained with methylene blue. The smears were examined with Nikon Ni-U Eclipse upright microscope imaging system using a color camera and manual stitching function. Normal RBCs appear pink, while Heinz bodies are visible as blue-black inclusions due to protein denaturation. Finally, by counting 300 to 500 RBCs, the proportion of Heinz body-positive RBCs can be determined.

2.4.4. Hematoxylin and eosin (H&E) staining

Mouse liver samples were fixed in 4% paraformaldehyde and embedded in paraffin blocks, which were further sectioned at 5 μm and stained with H&E. The sections were then examined using a Q-imaging digital camera and Axiophot 2 upright microscope (Axioplan 2, Zeiss) or Ni-U Eclipse upright microscope imaging system with a color camera and manual stitching function (Nikon).

2.4.5. Immunohistochemistry (IHC) analysis

IHC staining was carried out using a mouse and rabbit-specific HRP/DAB (ABC) detection IHC kit (Abcam, Cat. #AB64264) following the manufacturer's protocol. Briefly, mouse liver sections were deparaffinized, hydrated, and incubated in 10 mmol/L sodium citrate buffer at 98 °C for 20 min for antigen retrieval. After blocking with 10% goat serum for 1 h at room temperature, the sections were incubated with primary antibody against CD31 (Cell Signaling, Cat. #77966S), ferritin (Santa Cruz, Cat. #SC-376594), HO-1 (Santa Cruz, Cat. #SC-390991), VCAM-1 (Santa Cruz, Cat. #SC-13160), ACSL-4 (Santa Cruz, Cat. #SC-365230) or 4-HNE (Abcam, Cat. #AB48506) overnight at 4 °C. Then, the sections were incubated with biotinylated goat anti-polyvalent, followed by streptavidin peroxidase. The sections were then incubated with 3,3′-diaminobenzidine at room temperature. IHC images were taken by Q-imaging digital camera under Axiophot 2 upright microscope (Axioplan 2, Zeiss).

2.4.6. TUNEL staining

TUNEL staining was used to measure cell apoptosis of mouse liver sections following the manufacturer's protocol of the TUNEL assay kit (Abcam, Cat. #AB206386). The sections were examined with a Q-imaging digital camera and Axiophot 2 upright microscope (Axioplan 2, Zeiss).

2.4.7. Perls' Prussian blue staining

Mouse spleen samples were fixed in 4% paraformaldehyde and embedded in paraffin blocks, which were further sectioned at 5 μm and stained with Perls' Prussian blue. Briefly, the sections were incubated with an equal proportion of chloride acid (20%) and potassium ferrocyanide solution (2%) for 30 min at room temperature after deparaffinization and rehydration. Then, the sections were counterstained with 0.1% nuclear fast red solution for 5 min. The sections were examined with a Q-imaging digital camera and Axiophot 2 upright microscope (Axioplan 2, Zeiss). Blue staining was considered positive for iron presence.

2.5. Immunoprecipitation (IP)

IP of pyrrole-Hp protein or Hp−Hb complex was performed using Pierece™ Crosslink Magnetic IP/Co-IP kit (Thermo Fisher Scientific, Cat. #88805) according to the manufacturer's protocol. IP of Hp/pyrrole-Hp proteins was separated from RBCs or liver samples obtained from RTS-treated (60 mg/kg, 3 h) or control mice. Briefly, RBC protein or liver homogenates were prepared from RBCs or liver samples of RTS-treated or control mice by using the lysis buffer provided in the kit, respectively. The magnetic beads were crosslinked with 2 μg of anti-Hp (Santa Cruz, Cat. #Sc-390962) antibodies. RBCs, hepatic proteins or HepaRG cell medium were incubated with antibody-crosslinked resin at 4 °C overnight with gentle shaking to allow immune-capture of the target protein. Finally, the immune-captured proteins were isolated from the magnetic beads using elution buffer provided by the kit, and then re-suspended in sample loading buffer provided by the kit, denatured at 95 °C, and separated using SDS-PAGE followed by Western blot analysis.

2.6. Western blot analysis

Protein samples obtained from IP were separated by reducing SDS-PAGE using a 10% acrylamide resolving gel. Blots were transferred to nitrocellulose membranes, blocked, and incubated with individual primary antibodies, including anti-pyrrole-protein, which was developed to specifically recognize pyrrole moiety bound with proteins[25], anti-Hb (Santa Cruz, Cat. #Sc-21757), and anti-Hp antibodies (Santa Cruz, Cat. #Sc-390962), overnight at 4 °C, followed by horseradish peroxidase-conjugated secondary antibodies overnight at 4 °C. Protein bands were visualized using Azure Biosystems™ chemiluminescent substrate.

2.7. Covalent docking

The covalent docking studies were conducted using CovDock algorithm in Maestro 12.8 developed by Schrödinger, Inc. (New York, NY, USA). Dehydro-pyrrolizidine alkaloids (DHPA) as the ligand containing electrophilic carbonium functional group was prepared in Schrödinger's LigPrep module, the ionization states of ligands were generated and retained specified chiralities at pH 7.4, the energy was minimized under OPLS4 force field. Haptoglobin−Hemoglobin complex crystal structure (PDB:

4X0L) with a resolution of 2.05 Å was selected for covalent docking studies. The crystal structure was preprocessed using Protein Preparation Wizard module. All the solvent molecules were removed, and necessary hydrogens were added. The whole structure was minimized under OPLS4 force field before the hydrogen bond assignment optimization. Maestro's receptor grid generation panel was utilized to configure the grid generation job. The grid box was set at the centroid of selected residues with $\leq$6 Å length. Its workflow starts with a Glide noncovalent docking simulation using SP (standard precision), the ligand dock to a specific grid receptor with positional restraints to ensure the formation of covalent bond[26]. The specific amino acid residues were taken as reactive residues with nucleophilic functional groups interacting with electrophilic carbonium warhead on the ligand to form covalent bonds. The reaction pattern was defined by custom SMARTS pattern in Maestro. The covalent docking studies were conducted under the pose prediction docking mode to get more accurate pose conformation[27], the ranking of final covalent optimized structures was performed by comparing Prime energy scores and complex conformation. The conformation models were visualized using PyMol (PyMoL Molecular Graphics System, Version 1.6.0.) and LigPlot + software (Version v.2.2.8).

2.8. Correlation analysis

The correlation between patient plasma pyrrole−protein adduct levels and plasma cell-free hemoglobin levels was analyzed using Pearson correlation analysis. Due to the significantly high level of pyrrole−protein adduct, the data from patient No. 3 was considered as outlier data and excluded for the correlation analysis. The correlation was evaluated by Pearson correlation coefficient (r): $0.5 < r < 1$ as a strong positive correlation ($n = 29$).

2.9. Statistical analysis

Data are presented as mean ± standard deviation (SD) or standard error of mean (SEM). Statistical analysis was carried out using GraphPadPrism 10.1.0 software (GraphPad, USA). Prior to analysis, data were subjected to Normality and Lognormality tests. For normally distributed data, the statistical differences among experimental groups were analyzed by Student's t-test or one-way ANOVA followed by Bonferroni's test for two or multiple comparisons. For non-normal distributions, nonparametric tests (Kruskal−Wallis test) were applied. A P-value of less than 0.05 was considered statistically significant. Pearson correlation analysis was used to evaluate correlations, with a Pearson correlation coefficient (r) between 0.5 and 1 indicating a strong positive correlation.

3. Results

3.1. Hemolysis observed in PA-HSOS patients' plasma samples

This study included thirty PA-HSOS patients admitted between April 2019 to July 2020 (Fig. 1A and Table 1). Analysis of physiological and biochemical indices (Fig. 1B) revealed that 43.3% (13/30) of patients had abnormal ALT activity, 76.7% (23/30) had increased AST levels, and 43.3% (13/30) displayed elevated AKP levels, all indicating liver injury. Additionally, 63.3% (19/30) of patients showed reduced albumin levels, suggesting liver dysfunction or considerable albumin consumption. Platelet counts were low in 93.3% (28/30) of patients, and 86.7% (26/30) had prolonged prothrombin time, both suggesting a risk of intravascular bleeding. Elevated total bilirubin was present in 86.7% (26/30) of patients, with every patient showing elevated direct (conjugated) bilirubin levels, indicative of liver injury and jaundice. Furthermore, 53.3% (16/30) of patients had indirect (unconjugated) bilirubin levels exceeding the normal upper limit, which might be related to liver injury and hemolysis[28].

Histological analyses (Fig. 1C) and computed tomography (CT) scans (Fig. 1D) confirmed the presence of sinusoidal damage, intravascular bleeding, and congestion in the space of Disse, leading to portal hypertension. Plasma PPA levels, used as a biomarker for definitive PA-HSOS diagnosis[9], were detectable in all patients (Fig. 1 E), with significant variation (0.09−1.93 pmol/mg protein), likely due to differences in medication timing and PA intake amounts. Additionally, 93.3% (28/30) of patients exhibited abnormally high cell-free Hb levels (Fig. 1F), which showed a strong positive correlation with plasma PPA levels (Fig. 1G). These results suggest that hematopathy might play a crucial role in PA-HSOS pathogenesis.

3.2. RBC rupture occurs before LSEC damage induced by PA exposure

To further explore the pathology induced by PAs in RBCs, rat and mouse models of PA-HSOS were utilized with two representative toxic PAs, MCT and RTS. Directly incubating rat whole blood with dehydro-monocrotaline (DHM) *in vitro* resulted in significant hemolysis (Fig. 2A) and an increase in plasma Hb levels (Fig. 2B). However, neither RTS nor MCT induced hemolysis compared to the vehicle control. Moreover, the accumulation of PPA in RBCs was approximately 9 times greater than that in plasma (Fig. 2C), a trend also observed in RTS-exposed rats (Supporting Information Fig. S3), emphasizing the critical role of PPA formation in RBCs during PA-HSOS pathogenesis. Notably, with similar PPA levels, RTS exposure induced hemolysis in rats (Supporting Information Fig. S4). Under normal conditions, rat RBCs are rounded, smooth, and biconcave without clotting. However, PA exposure resulted in considerable morphological alterations, including changes in shape, size, and pattern, and RBC clotting (Fig. 2D). In the early stages of PA exposure, some RBCs lost central concave structure, elongating to an oval shape with increased size. Notably, some RBCs displayed central "slits", indicating RBC damage[29]. These findings suggest that PAs induce hemolysis. Given the comparable damage patterns caused by MCT and RTS, subsequent investigations focused exclusively on RTS. In mice, RTS exposure led to abnormal RBCs, such as microcytic cells, spherocytes, and "bite" cells, with an increase in Heinz bodies within 48 h (Fig. 2E and F, Supporting Information Fig. S5). Additionally, a significant reduction in G6PD activity was detected within the same period (Fig. 2G), indicating that G6PD might be a protein target for DHPA binding, leading to oxidative damage[30]. Collectively, these results demonstrate that PA exposure induces early hematopathy, and G6PD deficiency might be one of the causes resulting in RBC rupture.

3.3. Hemolysis is involved in both the initiation and progression of PA-HSOS

To further understand the role of hemolysis in the pathogenesis of PA-HSOS, mice were administered RTS at dosages of either 50 or 60 mg/kg. The findings indicated significantly higher levels of

PPA in RBCs compared to plasma (Fig. 3A). Histological analysis using H&E staining (Fig. 3B) showed mild sinusoidal dilation at 3 h and noticeable detachment of LSECs at 12 h post-exposure. The damage progressed gradually, showing RBC infiltration, obstruction, and hepatocyte apoptosis, ultimately culminating in HSOS at 48 h. To assess LSEC damage, expressions of CD31, a marker of endothelial cells, LYVE1, a specific marker of LSECs, VCAM-1, a marker for endothelial cell activation, and NO level were examined (Fig. 3C and D, Supporting Information Figs. S6 and S7). Consistent with H&E staining results, at 3 h after RTS exposure, LSECs remained relatively intact but showed a slight increase in VCAM-1-positive cells. The number of VCAM-1-positive LSECs increased significantly from 12 to 48 h, while CD31 expression dramatically decreased. TUNEL staining indicated sporadic hepatocyte apoptosis at 12 h and extensive hepatocyte apoptosis from 24 to 48 h after RTS exposure (Fig. 3E). Together, RTS caused LSEC activation and damage, followed by hepatocyte apoptosis. Interestingly, abnormal hepatic ferritin distribution was observed early on (Fig. 3F). In control mice, hepatic ferritin was evenly distributed, but 3 h after RTS exposure, ferritin relocalized around the central vein. This abnormal distribution became more pronounced at 12 h and persisted through 48 h. Concurrently, hepatic non-protein iron levels also increased, particularly at a higher RTS dose within the 3 to 48-h period (Fig. 3G). These observations suggested that RTS disrupts hemolytic iron homeostasis early on. Additionally, the expressions of ferroptosis-related proteins, including HO-1 (an inducer of intracellular oxidative damage)[31], 4-HNE (a product of lipid peroxidation damage)[32], and ACSL-4 (a sensitive monitor of ferroptosis)[33] were evaluated (Fig. 3H, Supporting Information Fig. S8). HO-1 and 4-HNE levels significantly upregulated from 12 to 48 h post-exposure. ACSL-4 expression increased in LSECs at 3 h and in both LSECs and hepatocytes from 12 to 48 h. These findings indicated that ferroptosis might be a downstream consequence of Hb accumulation and iron overload. To explore the role of ferroptosis in PA-HSOS, RTS-exposed mice were treated with liproxstatin-1 (Lip-1), a ferroptosis inhibitor. Lip-1 treatment notably alleviated RTS-induced hepatotoxicity, as evidenced by lower plasma ALT activity (Fig. 3I) and histological findings from H&E staining, IHC staining of CD31, and TUNEL staining (Fig. 3J), demonstrating that inhibiting ferroptosis with Lip-1 significantly mitigated LSEC damage and hepatocyte apoptosis. Overall, these results indicated that hemolytic iron homeostasis disorder and ferroptosis are critical factors in the initiation and progression of RTS-induced liver injury.

In PA-HSOS patients, elevated plasma ferritin levels were observed in 40.0% (12/30) of patients (Fig. 3K), linking iron overload to PA-HSOS pathogenesis. Additionally, decreased plasma transferrin receptor (TFR) levels, associated with iron overload[34], were found in 46.7% (14/30) of patients (Fig. 3K), further supporting the involvement of iron dysregulation in PA-HSOS development.

3.4. PA-induced Hp adduction exacerbates the accumulation of hemolytic products

Our preliminary study identified Hp, the scavenger protein for cell-free Hb, as the candidate for pyrrole-bound protein using MALDI-TOF mass-spectrometry analysis (Supporting Information Table S1). In the present study, a Co-IP assay was conducted to confirm the formation of the pyrrole−Hp adduct. Using an anti-Hp antibody, Hp was immunoprecipitated from mouse liver homogenates and detected by anti-Hp antibody in both control and RTS-treated samples. However, only the RTS-treated samples were recognized by the anti-pyrrole antibody (Fig. 4A, Supporting Information Fig. S9), confirming the presence of pyrrole−Hp adducts in RTS-exposed mice. Importantly, pyrrole−Hp adducts were also detected in the plasma of PA-HSOS patients but not in control samples (Fig. 4B, Supporting Information Fig. S10), indicating these adducts are presented in PA-exposed patients. Additionally, covalent docking studies revealed that DHPA forms a covalent bond with residue His183 in Hp (Fig. 4C).

To examine the functional impacts of Hp following DHPA binding, Hp was incubated with RTS in HepaRG cells (Fig. 4D, Supporting Information Fig. S11) or with DHM in a PBS buffer (Fig. 4E, Supporting Information Fig. S12) to generate pyrrole−Hp adducts, then excess Hb was added to form the Hp−Hb complex. Proteins containing Hp obtained through IP with an anti-Hp antibody were further analyzed for Hb expression using western blotting with an anti-Hb antibody. The results showed a significant reduction in Hp−Hb complex formation in both DHM- and RTS-exposed groups compared to the control group (Fig. 4D−G). These findings indicated that pyrrole−Hp adduction significantly impairs Hp function in clearing cell-free Hb by forming Hp−Hb complexes.

Moreover, cell-free Hb induced a time-dependent decline in human LSEC viability (Fig. 4H), while supplementation with Hp eliminated this adverse effect (Fig. 4I). Therefore, both RBC damage and Hp defunction contribute to the accumulation of cell-free Hb, leading to the initiation and progression of LSEC damage and subsequent PA-HSOS development. Thus, it is rational to hypothesize that endogenous Hp supplementation may offer a potential etiological therapeutic strategy for PA intoxication.

3.5. Hp supplement is an etiological therapy effectively against RTS-induced HSOS

To validate our hypothesis, mice received a single low or high dose of RTS, followed by 2 or 4 doses of Hp, respectively. Compared to the RTS-exposed group, Hp supplementation significantly reduced plasma ALT activity, indicating its protective role against RTS-induced hepatotoxicity (Fig. 5A). Notably, Hp supplementation did not affect PPA levels in plasma and RBCs (Fig. 5B), but significantly reduced serum Hb levels (Fig. 5C). The results suggest that Hp supplementation alleviated RTS-induced hepatotoxicity by removing cell-free Hb from the bloodstream, thereby mitigating its toxic effects.

At 48 h post-RTS exposure, consistent with prior observations (Fig. 3B−F, H), sinusoidal dilation (H&E), hemorrhage (H&E) (Fig. 5D), endothelial damage (CD31 and VCAM-1) (Fig. 5E and F), hepatocyte apoptosis (TUNEL) (Fig. 5G), iron homeostasis disruption (ferritin) (Fig. 5H) and ferroptosis (HO-1, 4-HNE, and ACSL-4) (Fig. 5I) were observed, particularly evident in mice exposed to the higher RTS dose relative to the lower dose. Remarkably, Hp supplements significantly improved RTS-induced hepatic hemorrhage, sinusoidal obstruction, cell apoptosis, and ferroptosis. Additionally, in the spleen, another crucial organ involved in iron recycling[35], iron expression within the red pulp was predominantly observed in control mice but was nearly absent in all RTS-exposed mice. However, Hp supplementation effectively restored splenic iron expression (Fig. 5J). Together with the semi-quantitative histological assessments (Fig. 5K), RTS exposure caused significant damage to LSEC and hepatocytes and

disrupted iron hemostasis. However, these impairments were ameliorated by Hp supplementation. In summary, Hp supplementation protected the liver from RTS-induced hepatotoxicity by eliminating toxic cell-free Hb and restoring both hepatic and splenic iron homeostasis.

4. Discussion

HILI has emerged as a significant contributor to drug-induced liver injury, with wide geographical variability due to the lack of standardized medicinal regulation[36-39]. PA-HSOS characterizes the distinct yet fatal HILI in China[6]. This study starts with the biochemical intoxication basis of most hepatotoxic reagents—protein adduction, while the key to specify the differential intoxication outcomes of different hepatotoxins is to identify their specific protein targets. Further verification of loss-of-function of the affected proteins underscores their characterized toxic effects on different liver cells, such as the unique toxic effects of PAs on LSECs[40-42]. Our previous studies revealed remarkably higher levels and longer duration of PPA in RBCs than that in the liver[16], and RBCs were found to serve as the carriers of DHPAs, facilitating transport of the reactive PA metabolites to extrahepatic organs[43]. These findings highlight the significance of investigating PA-related pathology in the circulating system, particularly RBCs.

This study was prompted by analysis of previously untested blood samples from PA-HSOS patients, where 53.3% (16/30) exhibited abnormally elevated levels of indirect bilirubin (Fig. 1B). While this increase could be attributed to liver injury, the potential contribution of hemolytic pathology warranted consideration. Additionally, cell-free hemoglobin (Hb) levels exceeded the normal upper limit in 93.3% (28/30) of patients and showed a positive correlation with blood pyrrole—protein adduct (PPA) levels (Fig. 1E—G), indicating PA-induced hematopathy in HSOS patients and suggesting an unidentified hemolysis-related mechanism underlying PA-HSOS pathogenesis. To investigate this hypothesis, we conducted *in vivo* and *in vitro* experiments to examine the effects of PA exposure on RBCs and its role in PA-HSOS pathogenesis.

Incubation of native PA compounds (RTS or MCT) with rat whole blood did not induce hemolysis. In contrast, DHPA (reactive PA metabolites) resulted in significant hemolysis caused by RBC protein adduction (Fig. 2A—C). Interestingly, hemolysis was also observed in rats at similar RBC PPA levels (Figs. S2 and S3). Given that the liver is the primary site for PA metabolic activation, the DHPA concentration within liver sinusoids is considerably high. Upon contact with RBCs, DHPA induces intravascular hemolysis in liver, causing *in situ* damage. Morphological examinations of PA-exposed RBCs revealed enlarged size, central "slits" and "bite" cells with increased expression of Heinz bodies and significantly decreased G6PD activity (Fig. 2G), which are representative RBC damage due to G6PD defunction[44,45]. Of note, these changes were observed as early as 3 h after PA exposure in both mice and rats (Fig. 2D—F), long before the onset of LSEC damage.

After unraveling the initiation of hemolysis, we also investigated the defense system against oxidative hemolytic products. Physiologically, cell-free Hb is scavenged by plasma Hp via forming an Hb—Hp complex and then removed by the reticuloendothelial system, primarily in the spleen, to maintain iron homeostasis[46]. However, defunctioning Hp due to adduction by DHPA caused accumulation of the highly oxidative cell-free Hb and hemolytic free iron, inducing LSEC damage (Fig. 4A—H)[47-49]. Correspondingly, NO level dramatically decreased with a time-dependent manner with 48 h post-RTS-exposure (Supporting Information Fig. S6), which might be attributed to RTS-induced LSEC defunctioning. Accordingly, significant LSEC damage was observed in RTS-exposed mice (Fig. 3C and D). Moreover, in the temporal sequence of HSOS pathogenesis, the hemolytic sinusoidal endothelial activation and damage were observed earlier than hepatocyte damage in mice: the expression of VCAM-1 was upregulated in LSECs within 3 h (the earliest observation time in this study), while hepatocyte apoptosis was not observed until 12 h post-RTS exposure (Fig. 3D and E). Our previous study revealed that LSECs are more sensitive to PA intoxication compared with hepatocytes[41], and cell-free Hb accumulation due to defunctioning Hp might be crucial factors. In addition, hepatic iron metabolism disorder was demonstrated by the alterations in hepatic ferritin distribution and early increase of hepatic non-protein iron (Fig. 3F and G). Consequently, endothelial ferroptosis, due to the hemolytic iron overload, also occurred in the early phase of RTS-induced hepatotoxicity (Fig. 3H). Notably, RBC and plasma PPA levels in mice treated with 60 mg/kg RTS showed slightly higher levels than those in mice treated with 50 mg/kg RTS (Fig. 3A) while hepatic iron levels and histological differences between these two groups are substantial. Given that PA-induced liver injury typically requires GSH depletion, this threshold effect explains why a slight elevation in PPA levels beyond the 50 mg/kg dose (where GSH is depleted) can precipitate significantly more severe histopathological outcomes. Inhibition of ferroptosis significantly alleviated RTS-induced hepatotoxicity (Fig. 3I and J). It should be noted that although Lip-1 is widely recognized for its role as an inhibitor of ferroptosis, Lip-1 also exhibits significant antioxidant properties[50], that can mitigate the secondary reactions of RTS-induced hematopathy and hepatotoxicity. Interestingly, a significant decrease in splenic iron was observed 48 h after RTS exposure (Fig. 5J and Supporting Information Fig. S13), suggesting a disorder of iron metabolism. Taken together, these results indicated that the hemolytic iron accumulation and disorder of iron homeostasis both contributed to PA-induced LSEC damage.

Considering that Hp is the critical scavenger of Hb (Fig. 4I), we proposed that endogenous Hp supplements could serve as an effective therapeutic intervention for PA intoxication. To avoid interfering with PPA formation, the biochemical basis of PA intoxication (Fig. 5B), we administered Hp to mice 3 h after RTS exposure, coinciding with the peak blood PPA levels (Fig. 3A). Notably, Hp supplements significantly alleviated RTS-induced hepatotoxicity by substantially reducing cell-free Hb levels (Fig. 5C). Furthermore, Hp supplements attenuated secondary hemolysis-related events, including ferroptosis and abnormalities in hepatic and splenic iron storage (Fig. 5H—J). Overall, this rescue study reinforces the role of hemolysis in the pathogenesis of PA-HSOS and highlights the therapeutic potential of Hp supplementation.

Finally, we validated the novel etiological mechanism in clinical samples. Consistent with the experimental findings, pyrrole—Hp adducts were detected in the plasma of PA-HSOS patients (Fig. 4B). Elevated levels of cell-free hemolytic products in these patients further implicated the clinical relevance of Hp defunction in PA-HSOS development. Interestingly, a retrospective study on PA-HSOS patients reported that hemosiderin deposition derived from damaged RBCs, as a common clinical manifestations of PA intoxication[51]. This observation supports our findings that the accumulation of hemolytic products and disruption of iron metabolism initiate LSEC damage, sinusoidal obstruction, and subsequent portal hypertension in PA-HSOS patients.

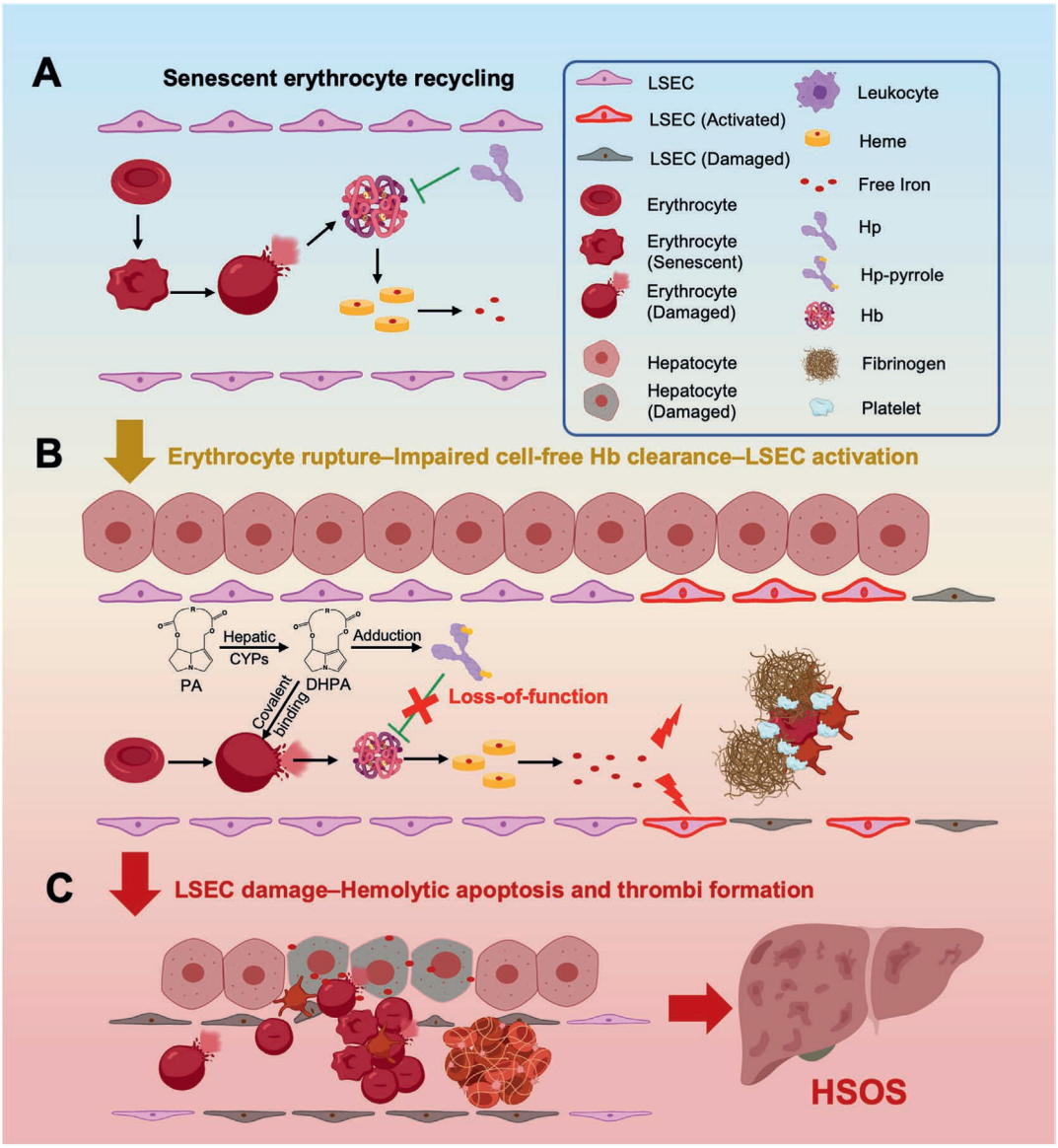

Figure 6 Schematic illustration of hemoglobin recycling and the pathologic role of PA exposure. Hemoglobin recycling under (A) physiological conditions and (B, C) pathogenesis of PA-induced HSOS.

5. Conclusions

This study delineated the etiological mechanism of PA-HSOS from a novel hematopathologic perspective: after PA exposure, the hepatocyte-derived DHPA caused RBC rupture and hemolysis, while the hemolytic products recycling (Fig. 6A) is also disrupted by DHPA, resulting in the accumulation of toxic Hb (Fig. 6B and C). Considering that the liver, as the primary site of PA metabolic activation, exhibits the highest DHPA concentrations, and the unique fenestrated structure of LSECs allows protein-bound xenobiotics to inflict localized damage, the accumulated toxic Hb within the hepatic sinusoid primarily damages LSECs through direct interaction. The presence of iron homeostasis disorder and direct toxicity of PPAs lead to hemorrhage and obstruction of space of Disse, along with hepatocyte apoptosis, culminating HSOS. Collectively, our findings suggest that exogenous Hp supplementation could serve as a potential etiological therapy for PA-HSOS.

Acknowledgements

This work was supported by the Research Grant Council of Hong Kong SAR (GRF Grant No. 14107719, China) and Guangdong Basic and Applied Basic Research Foundation (No. 2024A1515011705, China).

Author contributions

Zijing Song: conceptualization, data curation, formal analysis, investigation, methodology, project administration, software, validation, visualization, writing—original draft, and writing—review & editing. Yisheng He: conceptualization, data curation, formal analysis, funding acquisition, investigation, methodology, project administration, software, resources, visualization, writing—original draft, and writing—review & editing.

Wei Zhang: Data curation, formal analysis, investigation, methodology, project administration, resources, validation, visualization, writing—original draft, and writing—review & editing. Wei Lian: Conceptualization and methodology. Yueyang Pan: Data curation and visualization. Jiang Ma: Writing—original draft and writing—review & editing. Yuxuan Zhao: Data curation, formal analysis, and Software. Tianyang Huang: Data curation, Formal analysis, and software. Yuzheng Zhuge: Conceptualization, resources, and supervision. Ge Lin: Conceptualization, funding acquisition, methodology, project administration, resources, supervision, writing—original draft, and writing—review & editing.

Conflicts of interest

The authors declare no competing financial interests.

Appendix A. Supporting information

Supporting information to this article can be found online at https://doi.org/10.1016/j.apsb.2026.03.023.

References

1. DeLeve LD, McCuskey RS, Wang X, Hu L, McCuskey MK, Epstein RB, et al. Characterization of a reproducible rat model of hepatic veno-occlusive disease. *Hepatology* 1999;**29**:1779−91.
2. Chojkier M. Hepatic sinusoidal-obstruction syndrome: toxicity of pyrrolizidine alkaloids. *J Hepatol* 2003;**39**:437−46.
3. Mohty M, Malard F, Alaskar AS, Aljurf M, Arat M, Bader P, et al. Diagnosis and severity criteria for sinusoidal obstruction syndrome/veno-occlusive disease in adult patients: a refined classification from the European society for blood and marrow transplantation (EBMT). *Bone Marrow Transplant* 2023;**58**:749−54.
4. Corbacioglu S, Jabbour EJ, Mohty M. Risk factors for development of and progression of hepatic veno-occlusive disease/sinusoidal obstruction syndrome. *Biol Blood Marrow Transplant* 2019;**25**:1271−80.
5. Yang XQ, Ye J, Li X, Li Q, Song YH. Pyrrolizidine alkaloids-induced hepatic sinusoidal obstruction syndrome: pathogenesis, clinical manifestations, diagnosis, treatment, and outcomes. *World J Gastroenterol* 2019;**25**:3753−63.
6. Zhu L, Zhang CY, Li DP, Chen HB, Ma J, Gao H, et al. Tu-San-Qi (*Gynura japonica*): the culprit behind pyrrolizidine alkaloid-induced liver injury in China. *Acta Pharmacol Sin* 2021;**42**:1212−22.
7. Schrenk D, Gao L, Lin G, Mahony C, Mulder PPJ, Peijnenburg A, et al. Pyrrolizidine alkaloids in food and phytomedicine: occurrence, exposure, toxicity, mechanisms, and risk assessment—a review. *Food Chem Toxicol* 2020;**136**:111107.
8. Dubecke A, Beckh G, Lullmann C. Pyrrolizidine alkaloids in honey and bee pollen. *Food Addit Contam Part A Chem Anal Control Expo Risk Assess* 2011;**28**:348−58.
9. Mohabbat O, Younos MS, Merzad AA, Srivastava RN, Sediq GG, Aram GN. An outbreak of hepatic veno-occlusive disease in northwestern Afghanistan. *Lancet* 1976;**2**:269−71.
10. Robinson O, Want E, Coen M, Kennedy R, van den Bosch C, Gebrehawaria Y, et al. Hirmi Valley liver disease: a disease associated with exposure to pyrrolizidine alkaloids and DDT. *J Hepatol* 2014;**60**:96−102.
11. Chauvin P, Dillon JC, Moren A, Talbak S, Barakaev S. Heliotrope poisoning in Tadjikistan. *Lancet* 1993;**341**:1663.
12. Tandon BN, Tandon HD, Tandon RK, Narndranathan M, Joshi YK. An epidemic of veno-occlusive disease of liver in central India. *Lancet* 1976;**2**: 271−2.
13. Wang X, Qi X, Guo X. Tusanqi-related sinusoidal obstruction syndrome in China: a systematic review of the literatures. *Medicine (Baltim)* 2015;**94**:e942.
14. Fu PP, Xia Q, Lin G, Chou MW. Pyrrolizidine alkaloids—genotoxicity, metabolism enzymes, metabolic activation, and mechanisms. *Drug Metab Rev* 2004;**36**:1−55.
15. Lin G, Wang JY, Li N, Li M, Gao H, Ji Y, et al. Hepatic sinusoidal obstruction syndrome associated with consumption of Gynura segetum. *J Hepatol* 2011;**54**:666−73.
16. Ma J, Ruan J, Chen X, Li D, Yao S, Fu PP, et al. Pyrrole−hemoglobin adducts, a more feasible potential biomarker of pyrrolizidine alkaloid exposure. *Chem Res Toxicol* 2019;**32**:1027−39.
17. Ma J, Xia Q, Fu PP, Lin G. Pyrrole−protein adducts—a biomarker of pyrrolizidine alkaloid-induced hepatotoxicity. *J Food Drug Anal* 2018; **26**:965−72.
18. Zhuge Y, Liu Y, Xie W, Zou X, Xu J, Wang J, et al. Expert consensus on the clinical management of pyrrolizidine alkaloid-induced hepatic sinusoidal obstruction syndrome. *J Gastroenterol Hepatol* 2019;**34**:634−42.
19. Song Z, Lian W, He Y, Zhang C, Lin G. Targeting erythrocyte-mediated hypoxia to alleviate lung injury induced by pyrrolizidine alkaloids. *Arch Toxicol* 2023;**97**:819−29.
20. Zhu L, Xue J, He Y, Xia Q, Fu PP, Lin G. Correlation investigation between pyrrole−DNA and pyrrole−protein adducts in male ICR mice exposed to retrorsine, a hepatotoxic pyrrolizidine alkaloid. *Toxins* 2022;**14**:377.
21. Frimat M, Boudhabhay I, Roumenina LT. Hemolysis derived products toxicity and endothelium: model of the second hit. *Toxins* 2019;**11**:660.
22. Hulstein JJ, van Runnard Heimel PJ, Franx A, Lenting PJ, Bruinse HW, Silence K, et al. Acute activation of the endothelium results in increased levels of active von Willebrand factor in hemolysis, elevated liver enzymes and low platelets (HELLP) syndrome. *J Thromb Haemost* 2006;**4**:2569−75.
23. Schaer CA, Deuel JW, Bittermann AG, Rubio IG, Schoedon G, Spahn DR, et al. Mechanisms of haptoglobin protection against hemoglobin peroxidation triggered endothelial damage. *Cell Death Differ* 2013;**20**:1569−79.
24. Hammour MM, Othman A, Aspera-Werz R, Braun B, Weis-Klemm M, Wagner S, et al. Optimisation of the HepaRG cell line model for drug toxicity studies using two different cultivation conditions: advantages and limitations. *Arch Toxicol* 2022;**96**:2511−21.
25. Li N, Zhang F, Lian W, Wang H, Zheng J, Lin G. Immunoassay approach for diagnosis of exposure to pyrrolizidine alkaloids. *J Environ Sci Health C Environ Carcinog Ecotoxicol Rev* 2017;**35**:127−39.
26. Toledo Warshaviak D, Golan G, Borrelli KW, Zhu K, Kalid O. Structure-based virtual screening approach for discovery of covalently bound ligands. *J Chem Inf Model* 2014;**54**:1941−50.
27. Scarpino A, Ferenczy GG, Keseru GM. Binding mode prediction and virtual screening applications by covalent docking. *Methods Mol Biol* 2021;**2266**:73−88.
28. Guerra Ruiz AR, Crespo J, Lopez Martinez RM, Iruzubieta P, Casals Mercadal G, Lalana Garces M, et al. Measurement and clinical usefulness of bilirubin in liver disease. *Adv Lab Med* 2021;**2**:352−72.
29. Melzak KA, Spouge JL, Boecker C, Kirschhofer F, Brenner-Weiss G, Bieback K. Hemolysis pathways during storage of erythrocytes and inter-donor variability in erythrocyte morphology. *Transfus Med Hemother* 2021;**48**:39−47.
30. Opsahl M, Chen W. Blister and bite cells in G6PD deficiency. *Int J Lab Hematol* 2022;**44**:55−6.
31. Tang ZM, Ju YH, Dai XC, Ni N, Liu Y, Zhang DD, et al. HO-1-mediated ferroptosis as a target for protection against retinal pigment epithelium degeneration. *Redox Biol* 2021;**43**:101971.
32. Tang D, Chen X, Kang R, Kroemer G. Ferroptosis: molecular mechanisms and health implications. *Cell Res* 2021;**31**:107−25.
33. Yuan H, Li XM, Zhang XY, Kang R, Tang DL. Identification of ACSL4 as a biomarker and contributor of ferroptosis. *Biochem Bioph Res Co* 2016;**478**:1338−43.
34. Khumalo H, Gomo ZA, Moyo VM, Gordeuk VR, Saungweme T, Rouault TA, et al. Serum transferrin receptors are decreased in the presence of iron overload. *Clin Chem* 1998;**44**:40−4.
35. Slusarczyk P, Mleczko-Sanecka K. The multiple facets of iron recycling. *Genes* 2021;**12**:1364.

36. Larrey D, Faure S. Herbal medicine hepatotoxicity: a new step with development of specific biomarkers. *J Hepatol* 2011;**54**:599−601.
37. European Association for the Study of the Liver. EASL clinical practice guidelines: drug-induced liver injury. *J Hepatol* 2019;**70**:1222−61.
38. The Lancet Gastroenterology H. Herbal and dietary supplements: unregulated hepatotoxicity. *Lancet Gastroenterol Hepatol* 2024;**9**:965.
39. Xiao X, Tang J, Mao Y, Li X, Wang J, Liu C, et al. Guidance for the clinical evaluation of traditional Chinese medicine-induced liver injury issued by China Food and Drug Administration. *Acta Pharm Sin B* 2019;**9**:648−58.
40. Ma J, Li M, Li N, Chan WY, Lin G. Pyrrolizidine alkaloid-induced hepatotoxicity associated with the formation of reactive metabolite-derived pyrrole−protein adducts. *Toxins* 2021;**13**:723.
41. Yang M, Ruan J, Fu PP, Lin G. Cytotoxicity of pyrrolizidine alkaloid in human hepatic parenchymal and sinusoidal endothelial cells: firm evidence for the reactive metabolites mediated pyrrolizidine alkaloid-induced hepatotoxicity. *Chem Biol Interact* 2016;**243**:119−26.
42. He Y, Ma J, Fan X, Ding L, Ding X, Zhang QY, et al. The key role of gut−liver axis in pyrrolizidine alkaloid-induced hepatotoxicity and enterotoxicity. *Acta Pharm Sin B* 2021;**11**:3820−35.
43. He Y, Lian W, Ding L, Fan X, Ma J, Zhang QY, et al. Lung injury induced by pyrrolizidine alkaloids depends on metabolism by hepatic cytochrome P450s and blood transport of reactive metabolites. *Arch Toxicol* 2021;**95**:103−16.
44. Tyrrell L, Rose G, Shukri A, Kahwash SB. Morphologic changes in red blood cells: an illustrated review of clinically important light microscopic findings. *Malays J Pathol* 2021;**43**:219−39.
45. Yoo D, Lessin LS. Drug-associated "bite cell" hemolytic anemia. *Am J Med* 1992;**92**:243−8.
46. Lim SK, Ferraro B, Moore K, Halliwell B. Role of haptoglobin in free hemoglobin metabolism. *Redox Rep* 2001;**6**:219−27.
47. Meegan JE, Bastarache JA, Ware LB. Toxic effects of cell-free hemoglobin on the microvascular endothelium: implications for pulmonary and nonpulmonary organ dysfunction. *Am J Physiol Lung Cell Mol Physiol* 2021;**321**:L429−39.
48. Rifkind JM, Mohanty JG, Nagababu E. The pathophysiology of extracellular hemoglobin associated with enhanced oxidative reactions. *Front Physiol* 2014;**5**:500.
49. Fibach E, Rachmilewitz EA. Iron overload in hematological disorders. *Presse Med* 2017;**46**:e296−305.
50. Zilka O, Shah R, Li B, Friedmann Angeli JP, Griesser M, Conrad M, et al. On the mechanism of cytoprotection by Ferrostatin-1 and Liproxstatin-1 and the role of lipid peroxidation in ferroptotic cell death. *ACS Cent Sci* 2017;**3**:232−43.
51. Liu F, Rong X, Guo H, Xu D, Liu C, Meng L, et al. Clinical characteristics, CT signs, and pathological findings of pyrrolizidine alkaloids-induced sinusoidal obstructive syndrome: a retrospective study. *BMC Gastroenterol* 2020;**20**:30.